A threedimensional quantum mechanical study of vibrationally resolved charge transfer processes in H++H2 at E cm=20 eV

Michael Baer, Gereon NiednerSchatteburg, and J. Peter Toennies

Citation: The Journal of Chemical Physics **91**, 4169 (1989); doi: 10.1063/1.456794
View online: http://dx.doi.org/10.1063/1.456794
View Table of Contents: http://scitation.aip.org/content/aip/journal/jcp/91/7?ver=pdfcov
Published by the AIP Publishing

A three-dimensional quantum mechanical study of vibrationally resolved charge transfer processes in $H^+ + H_2$ at $E_{cm} = 20$ eV

Michael Baer,[a] Gereon Niedner-Schatteburg,[b] and J. Peter Toennies
Max-Planck-Institut für Strömungsforschung, Bunsenstr. 10, 3400 Göttingen, Federal Republic of Germany

(Received 15 November 1988; accepted 23 June 1989)

A three-dimensional quantum mechanical study of vibrational state resolved differential cross sections for the direct inelastic and charge transfer channels of the $H^+ + H_2$ system has been carried out at $E_{cm} = 20$ eV using the infinite order sudden approximation (IOSA). Steric factors, opacity functions, angular distributions, and integral cross sections are calculated. The integral cross sections are in very good agreement with recent experimental results, whereas the angular distributions agree only partially with the experiments. A further comparison of both the theoretical and experimental results with semi-classical calculations based on the usual trajectory surface hopping method revealed that the present quantum results provide a better description of the experimental observations. The likely shortcomings of the semiclassical method are discussed.

I. INTRODUCTION

At the present time surprisingly little is known about the dynamics of charge transfer collisions in which one of the partners is a molecule.[1–3] Charge transfer belongs to the broader class of collision processes involving transitions between two or more potential hypersurfaces. These transitions usually occur in well defined regions of configuration space where the diabatic potential energy surfaces cross each other and the Born–Oppenheimer approximation breaks down. Such crossing processes invariably occur in reactive or nonreactive collisions of open shell systems and in most ion–molecule collisions. Thus the study of surface crossing processes in molecular collisions is of fundamental importance for an understanding of reaction dynamics.

There are several reasons for the lack of knowledge of molecular charge transfer. To study this process experimentally it is necessary to either employ a mass spectrometer to identify the newly formed product ions or selectively detect the fast neutral species produced. If one wants to acquire state-to-state information means for state selection must be provided as well. The theory is also more involved than in case of adiabatic (single surface) processes. A knowledge of the different potential hypersurfaces is required and the dynamics must not only follow the various surfaces but, in addition, adequately account for the transition from one surface to the next. In view of these complications most theories have relied on the semiclassical approach.[3] One particular method due to Bauer, Fisher, and Gilmore[4] is based on the diabatic vibrational states which interact at the crossing points. Another method is the trajectory surface hopping model (TSHM) which was first suggested by Bjerre and Nikitin[5] and later extensively used to study various systems.[3,6,7] In the TSHM the trajectories are treated classically, and in the regions where the diabatic potential surfaces cross the transition probabilities are approximated by the Landau–Zener formula[8,9] which describes atom–ion charge transfer. The success of this approach in explaining the measured energy dependence of cross sections of the $H^+ + D_2$ system is somewhat surprising[7] since both, the classical trajectory method and the Landau-Zener formula when applied independently, in many cases, yield erroneous results. Baer and co-workers[10–12] have developed a quantum mechanical approach which in principle treats the transitions between surfaces correctly by utilizing a number of judiciously chosen adiabatic–diabatic transformations. With this method it is possible to carry out realistic quantum mechanical calculations for molecular charge transfer processes.

The present study was motivated by the recent availability of vibrationally resolved differential cross sections for the inelastic and charge transfer channels for the collision processes[13]:

$$H^+ + H_2(v_i = 0) \rightarrow H^+ + H_2(v_f), \quad \Delta E_0 = 0, \tag{1a}$$

$$\rightarrow H^0 + H_2^+(v_f'), \quad \Delta E_0 = 1.83 \text{ eV}. \tag{1b}$$

The experiments were performed at an energy of $E_{Lab}\,(\cong 3/2\,E_{cm}) = 30$ eV and encompassed scattering angles up to 20 deg. At these high collision energies the reactive channel has a very low probability[13] and can be completely neglected.

With only two electrons, this is the simplest of all ion molecule collision systems. The potential hypersurface has been extensively studied and it has been found that the computationally convenient diatomics-in-molecules (DIM) potential is reasonably accurate.[14] This potential was used by Niedner *et al.*[13] within the framework of the TSHM to calculate differential and total cross sections for direct comparison with the above experiment. The agreement between experiment and theory was reasonably good in some respects, but serious disagreements in particular for the charge transfer process were noticed as well. Consequently, the aim of

[a] Permanent address: Soreq Nuclear Research Center, Yavne 70600, Israel.
[b] Present address: Dept. of Chemistry, University of California, Berkeley, CA 94720.

 0021-9606/89/194169-14$02.10

the present investigation was to apply the quantum mechanical approach to the calculation of the state to state differential cross sections for a direct comparison with both the experiments and the TSHM calculations. This treatment was made possible by the recent extension of the infinite order sudden approximation (IOSA) to charge transfer processes.[12]

The article starts with a detailed description of the salient features of the potential hypersurfaces employed. Next the dynamical theory is outlined and the quantities calculated are defined. In the following section details of the numerical calculations are presented. Finally the calculated quantities are compared with the experiments and the TSHM calculations. The paper closes with a summary and discusses further improvements in the theory.

II. THE POTENTIAL

A. The DIM potential matrix

The potential hypersurface employed in the present calculations is the DIM potential as first suggested by Ellison[15] and later applied by Preston and Tully.[14(a)] Comparison with the recent more accurate *ab initio* calculations[16–18] for the lower adiabatic surface reveals a number of inaccuracies of the DIM surface. Nevertheless the DIM potential was used in this work for the following reasons. (1) This potential is the only one which provides convenient expressions for the nonadiabatic coupling terms. (2) It has been used in all previous charge transfer studies so that the new results obtained here can be compared with those calculations.

The 3×3 DIM potential matrix includes the gerade and the ungerade states $^2\Sigma_g^+$ and $^2\Sigma_u^+$, respectively, of the H_2^+ molecule and the ground state $^1\Sigma_g^+$ of the H_2 molecule. Figures 1(a), 1(b), and 1(c) presents three-dimensional views of the diabatic potential hypersurfaces (i.e. the diagonal elements) for three different bond distances. The two spatial coordinates are the translational coordinate R and the orientation angle γ. At $r = 0.74$ Å [Fig. 1(a)] which is the equilibrium bond length of H_2 the asymptotic ($R\rightarrow\infty$) difference between the two surfaces is the vertical difference between the ionization potential of H_2 and of H (13.69 eV). At $r = 1.32$ Å [Fig. 1(b)] the asymptotic difference vanishes but the surfaces diverge as R becomes smaller than 3 Å. With further increase in bond distance [Fig. 1(c)] the two surfaces pass through each other and form a crossing seam. In addition to the three-dimensional views of Figs. 1(a) to 1(c) two plots of the equipotential lines of the diabatic ground state potential of H_3^+ are shown as a function of R and γ, while the intramolecular H_2 bond distance is held at $r = 0.74$ Å [Fig. 1(d)] and $r = 1.32$ Å [Fig. 1(e)]. This sequence of potential hypersurfaces shows the importance of bond stretching in facilitating the charge transfer process.

B. The adiabatic–diabatic transformation

Although the DIM approach yields three adiabatic potential surfaces it is sufficient in the dynamical treatment to consider only the two lowest adiabatic surfaces including the corresponding nonadiabatic coupling terms. However, due to numerical instabilities the dynamical calculations had to be carried out within the diabatic framework. Thus, one is forced to apply a series of adiabatic-to-diabatic transformations to eliminate the nonadiabatic coupling terms and obtain the corresponding diabatic framework.

The adiabatic–diabatic transformations employed in the present study have been discussed extensively in the literature[1,10–12] (see also Ref. 19) but for the sake of completeness will be briefly repeated here. The Schrödinger equation to be considered is

$$H\Psi(e,n) = E\Psi(e,n), \tag{2}$$

where e and n denote electronic and nuclear coordinates, respectively, and the Hamiltonian H will be written as

$$H = T_n + H_e. \tag{3}$$

Here T_n is the nuclear kinetic energy and H_e accounts for both the electronic kinetic energy and the potential energy. Following Born and Oppenheimer[20] the wave function $\psi(e,n)$ can be expanded in the form (assuming a two state case)

$$\Psi(e,n) = \sum_{i=1}^{2}\rho_i(e,n)\chi_i(n), \tag{4}$$

where the $\rho_i(e,n)$ are the eigenfunctions of H_e and account for the electronic states of the system for a given nuclear configuration. Substituting Eq. (4) into Eq. (3) leads to the two adiabatic surfaces $V_i(R,r,\gamma)$ corresponding to $i = 1,2$ and the nonadiabatic coupling matrices $\tau^{(1)}$ and $\tau^{(2)}$ defined as

$$\tau_{ji}^{(1)} = \langle \rho_j|\nabla\rho_i\rangle, \tag{5a}$$

$$\tau_{ji}^{(2)} = \langle \rho_j|\nabla^2\rho_i\rangle. \tag{5b}$$

Here the derivative operator vector ∇ is

$$\nabla = \left(\frac{\partial}{\partial R},\frac{\partial}{\partial r},\frac{1}{a}\frac{\partial}{\partial\gamma}\right), \tag{6}$$

where R and r are the mass scaled translational and vibrational coordinates, γ is the orientation angle defined as

$$\gamma = \cos^{-1}(\hat{R}\cdot\hat{r}) \tag{7}$$

and a can be shown to be[1]

$$a = \frac{r\cdot R}{(R^2+r^2)^{1/2}}. \tag{8}$$

To solve the resulting nuclear Schrödinger equation presents severe computational difficulties which originate from singularties in $\tau_{ij}^{(1)}$ encountered in the asymptotic region. Moreover the calculation of $\tau_{ji}^{(1)}$ and $\tau_{ij}^{(2)}$ requires additional calculations involving the first and second derivative matrices of the electronic wave functions with respect to the nuclear coordinates. As was shown elsewhere[10,19] these difficulties can be avoided by a series of transformations to a different set of nuclear wave functions η,

$$\chi = A\eta. \tag{9}$$

If A is chosen to fulfill the following vector equation:

$$\nabla A + \tau^{(1)}A = 0, \tag{10}$$

it can be shown that A is orthogonal. Then the resulting nuclear Schrödinger equation becomes

$$[\,T_n\eta + (W - E\,]\eta = 0, \tag{11}$$

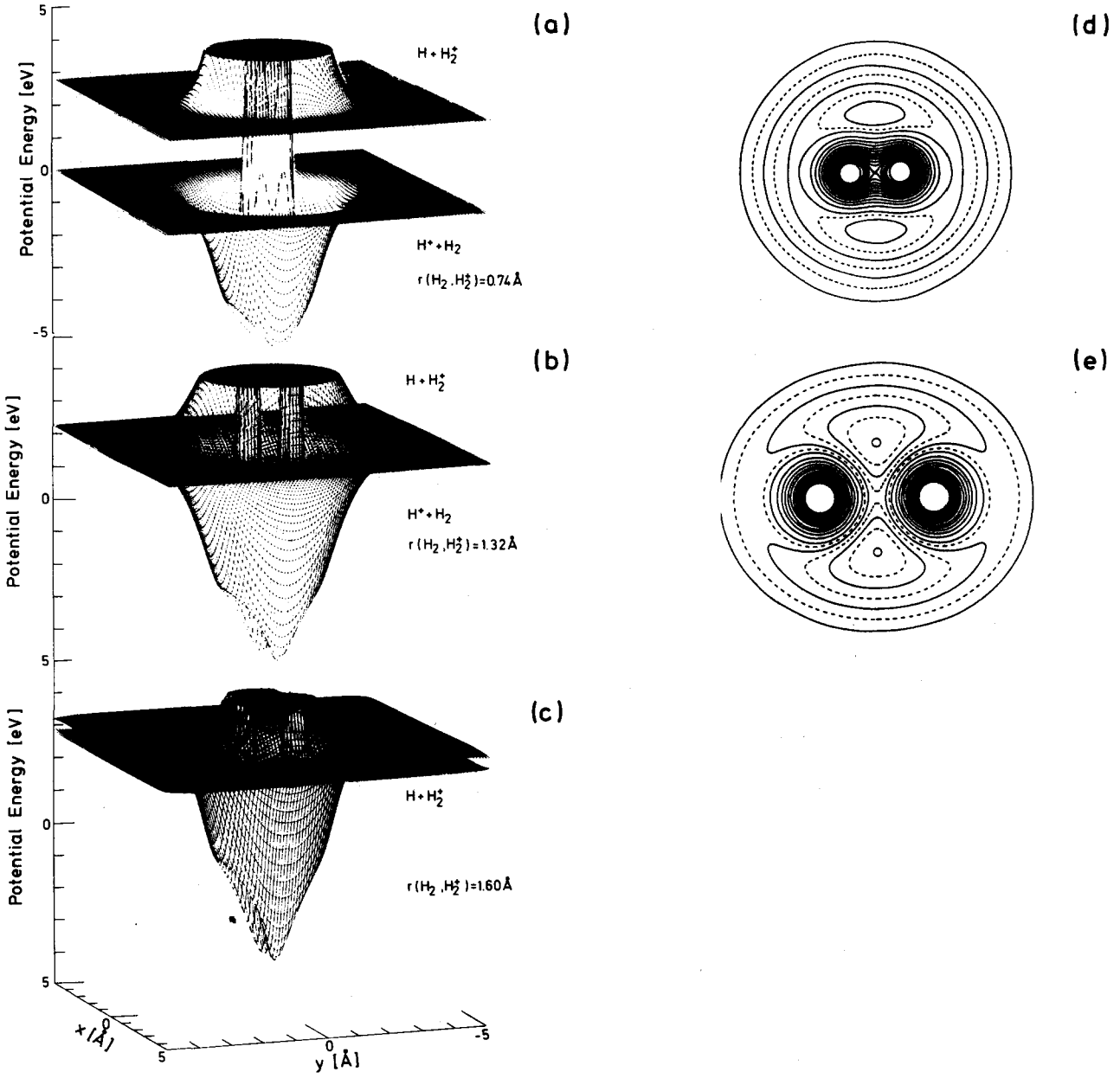

FIG. 1. The two lowest adiabatic surfaces of the $(H + H_2)^+$ system for fixed interatomic distances r of the diatomic molecule (or ion). The drawings (a) to (c) give the potential energy V in the z direction as a function of the distance R and the molecular orientation angle γ. R and γ lie in the x, y plane. Moreover, (d) and (e) give two contour plots of the lower surface. The molecular bond axis of the diatom (or ion) is along the y direction in all figures. (a),(d) $r = 0.74$ Å (the equilibrium bond length of H_2). (b),(e) $r = 1.32$ Å (the position of the seam at the asymptotic region). (c) $r = 1.6$ Å.

where W is the diabatic potential matrix defined as

$$\mathsf{W} = \mathsf{A}^*\mathsf{V}\mathsf{A}. \tag{12}$$

Here V is the diagonal adiabatic potential matrix. The final outcome of this procedure is that the nonadiabatic coupling terms are transformed into diabatic potential couplings.

It is important to emphasize that since the interaction potential is obtained by the DIM method, the adiabatic–diabatic transformation is complete and does not involve any approximation (see also Ref. 14).

Since A is orthogonal it can be written for the two surfaces case as

$$\mathsf{A} = \begin{pmatrix} \cos\alpha & \sin\alpha \\ -\sin\alpha & \cos\alpha \end{pmatrix}, \tag{13}$$

where the transformation angle α is given by[1,10]

$$\alpha(r,R,\gamma) = \alpha_0 + \int_{r_0}^{r} \tau_r^{(1)}(R,r,\gamma)dr + \int_{R_0}^{R} \tau_R^{(1)}(R,r_0,\gamma)dR + \int_{\gamma_0}^{\gamma} \tau_\gamma^{(1)}(R_0,r_0,\gamma)d\gamma. \tag{14}$$

Note that $\tau^{(2)}$ no longer enters into the problem since it has been eliminated in the transformation of Eq. (9).

As mentioned above, we in fact consider only two adiabatic surfaces $V_i, i = 1,2$ (see Fig. 1) and therefore the corresponding diabatic potential surfaces W_j $(j = 1,2)$ and the diabatic coupling term W_{12} are easily obtained [see Eq. (12)]:

$$W_1 = V_1 \cos^2\alpha + V_2 \sin^2\alpha, \tag{15a}$$

$$W_2 = V_1 \sin^2\alpha + V_2 \cos^2\alpha, \tag{15b}$$

$$W_{12} = \tfrac{1}{2}(V_2 - V_1)\sin^2\alpha. \tag{15c}$$

In the limit of $R \to \infty$ the transformation angle α becomes a step function as result of the nonadiabatic coupling term becoming a δ function.[1,10] This asymptotic behavior of α guarantees the correct asymptotic limit of the potential when one of the atoms is removed to infinity. Namely, it leads to the correct diatomic potential of the segments of $H_2(W_1)$ and of $H_2^+(W_2)$. Thus:

$$W_1 = \begin{cases} V_1; & r < r_s \\ V_2; & r > r_s \end{cases} \quad (R \to \infty), \tag{16a}$$

$$W_2 = \begin{cases} V_1; & r > r_s \\ V_2; & r < r_s \end{cases} \quad (R \to \infty), \tag{16b}$$

and

$$W_{12} = W_{21} = 0 \quad (R \to \infty). \tag{16c}$$

In the present case r_s is the intersection point between the shifted diatomic potentials of H_2 and H_2^+ which is found to be at $r_s = 1.32$ Å.

In actual practice it has been found to be expedient to carry out another transformation in order to avoid numerical instabilities in the propagation procedure of the Schrödinger equation. The derived transformation is one that yields $\overline{W}_{12}[r(R),R] \equiv 0$ along an *a priori* chosen path $r = r(R)$. This transformation produces a representation which is as close as possible to the original adiabatic representation still without introducing the nonadiabatic coupling terms. In the present case the path was chosen to be a *straight* line along the R axis namely:

$$r(R) = r_{\text{ad}}, \tag{17}$$

where r_{ad} is a constant which in the present calculation was taken to be $r_{\text{ad}} = 0.8$ Å. This line is very close to the minimum energy path.

III. THE INFINITE ORDER SUDDEN APPROXIMATION (IOSA)

A. The Schrödinger equation

As mentioned in the Introduction, the numerical treatment is carried out within the framework of the infinite order sudden approximation (IOSA).[12,21–24] The general conditions for the validity of the IOSA were presented and discussed extensively elsewhere[12] and will not be repeated here. The $(H + H_2)^+$ system differs from many systems studied previously in that the interaction potential is almost isotropic. In general, this feature makes the IOSA particularly valid even for systems for which it might not otherwise expected to be accurate. As a result, both the orbital angular momenta and the internal angular momenta become decoupled thereby avoiding the complicated vector coupling algebra and the additional computational effort associated with it. The IOSA has been frequently studied in the past and has been shown to be a reliable approximation under various conditions.[25] Recently it has also been applied to charge transfer processes and reasonable agreement with experiment was obtained.[12,26]

In the case of H_3^+ the γ dependence of the potential hypersurfaces is weak. This can be seen by examining the two relevant adiabatic surfaces for a fixed vibrational distance but varying translational distance and orientation angle. Three such situations are shown in Fig. 1 and it is observed that except for a short range of R (when R becomes less than 1 Å) the potential is rather isotropic. The fact that the potential is not isotropic near the repulsive part of the potential is not expected to affect much the path of either the approaching or the receding particles but still may have an effect on the vibrational excitation and the charge transfer processes. Consequently the calculations are not done for one single value of γ but are repeated for a series of γ values, and the final physical results are obtained following an integration over γ.

As was mentioned earlier the introduction of the IOSA simplifies significantly the Schrödinger equation to be solved. In the present case, the two coupled Schrödinger equations can be shown to take the form[12]

$$\left[-\frac{\hbar^2}{2\mu}\left\{\frac{\partial^2}{\partial R^2}+\frac{\partial^2}{\partial r^2}\right\} + W_{11} + \frac{\hbar^2}{2\mu}\frac{l(l+1)}{R^2} - E\right] \times \Psi_1(R,r,\gamma) + W_{12}\Psi_2(R,r,\gamma) = 0, \tag{18a}$$

$$\left[-\frac{\hbar^2}{2\mu}\left\{\frac{\partial^2}{\partial R^2}+\frac{\partial^2}{\partial r^2}\right\} + W_{22} + \frac{\hbar^2}{2\mu}\frac{l(l+1)}{R^2} - E\right] \times \Psi_2(R,r,\gamma) + W_{12}\Psi_1(R,r,\gamma) = 0. \tag{18b}$$

In the previous chapter we showed that in order to obtain the diabatic equations [i.e., Eqs. (18)] the transformation angle $\alpha(R,r,\gamma)$ has to be calculated at each step. Fortunately in the IOSA the calculation of α simplifies because $\alpha(R,r,\gamma)$ can now be calculated independently for each value of γ. Therefore the last term in Eq. (14) is a constant that can be added to α_0 to form a new constant. Thus, within the IOSA, the equation for $\alpha(R,r,\gamma)$ is

$$\alpha(R,r,\gamma) = \alpha_0 + \int_{r_0}^{r} dr\, \tau_r^{(1)}(R,r,\gamma) + \int_{R_0}^{R} dR\, \tau_R^{(1)}(R,r_0,\gamma). \tag{14'}$$

As in a previous study of $(Ar + H_2)^+$ [12,26] the $\tau_R^{(1)}$ and $\tau_r^{(1)}$ are calculated from the ordinary interatomic coupling terms $\tau_{r_i}^{(1)}$, $i = 1,2,3$ using the chain rule

$$\tau_x^{(1)} = \sum_{i=1}^{3} \tau_{r_i}^{(1)} \frac{\partial r_i}{\partial x}; \quad x = R,r. \tag{19}$$

Recalling the relation

$$r_1^2 = R^2 + \tfrac{1}{4}r^2 - rR\cos\gamma, \tag{20a}$$

$$r_2 = r, \tag{20b}$$

$$r_3^2 = R^2 + \tfrac{1}{4}r^2 + rR\cos\gamma, \tag{20c}$$

we get for the general case

$$\tau_R^{(1)} = \frac{R - \frac{1}{2}r\cos\gamma}{r_1}\tau_{r_1}^{(1)} + \frac{R + \frac{1}{2}r\cos\gamma}{r_3}\tau_{r_3}^{(1)}, \tag{21a}$$

$$\tau_r^{(1)} = \frac{r - 2R\cos\gamma}{4r_1}\tau_{r_1}^{(1)} + \tau_{r_2}^{(1)} + \frac{r + 2R\cos\gamma}{4r_3}\tau_{r_3}^{(1)}. \tag{21b}$$

The nonadiabatic coupling terms $\tau_{r_i}^{(1)}$ for $i = 1,2,3$ were calculated using the Hellmann Feynman theorem[1]:

$$\tau_p^{(1)} = \frac{\mathbf{A}_2^*(\partial \mathsf{H}/\partial p)\mathbf{A}_1}{V_2 - V_1}; \quad p = r_1, r_2, r_3, \tag{22}$$

where $\mathbf{A}_1$ and $\mathbf{A}_2$ are the eigenvectors associated with the eigenvalues V_1 and V_2, respectively, and H is the DIM matrix.

Calculated values of $\alpha(R,r,\gamma)$ as a function of r for $\gamma = 0°, 30°, 60°$, and $90°$ are shown in Fig. 2 for $R = 1, 2, 3, 4$, and 5 Å. Since the dependence of α on γ is not very pronounced it was neglected altogether. With this assumption the angle $\alpha(R,r)$ was fitted to an analytical expression of the form

$$\alpha = \alpha_0(R) + \bar{\alpha}(R)\{1 + \tanh q(R)[r - r_s(R)]\}. \tag{23}$$

Here the four R-dependent functions $\alpha_0(R)$, $\bar{\alpha}(R)$, $q(R)$, and $r_s(R)$ are expressed analytically in terms of parameters which were determined by a fit to the exact DIM calculated values of $\alpha(R,r)$:

$$\alpha_0(R) = \alpha_{00}|R_0 - R|^{n_0};$$
$$\alpha_{00} = 0.017; \quad R_0 = 5\ \text{Å}; \quad n_0 = 2.8, \tag{24a}$$
$$\bar{\alpha}(R) = -\bar{\alpha}_0 + \bar{\alpha}_1 R + \bar{\alpha}_2 R^{\bar{n}};$$
$$\bar{\alpha}_0 = 0.07;$$
$$\bar{\alpha}_1 = 0.18;$$
$$\bar{\alpha}_2 = 5\times 10^{-6}; \quad \bar{n} = 6, \tag{24b}$$
$$r_s(R) = r_{s_1} + r_{s_2}[1 + \tanh(R - r_{s_3})];$$
$$r_{s_1} = 0.76; \quad r_{s_2} = 0.283; \quad r_{s_3} = 27, \tag{24c}$$
$$q(R) = q_0 + q_1 R + q_2 R^{n_q}; \quad q_0 = 0.89;$$
$$q_1 = 0.25; \quad q_2 = 1.5\times 10^{-4}; \quad n_q = 6.6. \tag{24d}$$

Values of α as calculated from Eqs. (23) and (24) are compared with the corresponding DIM values in Fig. 2, and the agreement is seen to be good. A three-dimensional view of $\alpha(R,r)$ is presented in Fig. 3. In the limit of $R \to \infty$, α goes over, as a function of r, to a well defined step function. This corresponds to a δ function for the nonadiabatic coupling terms.

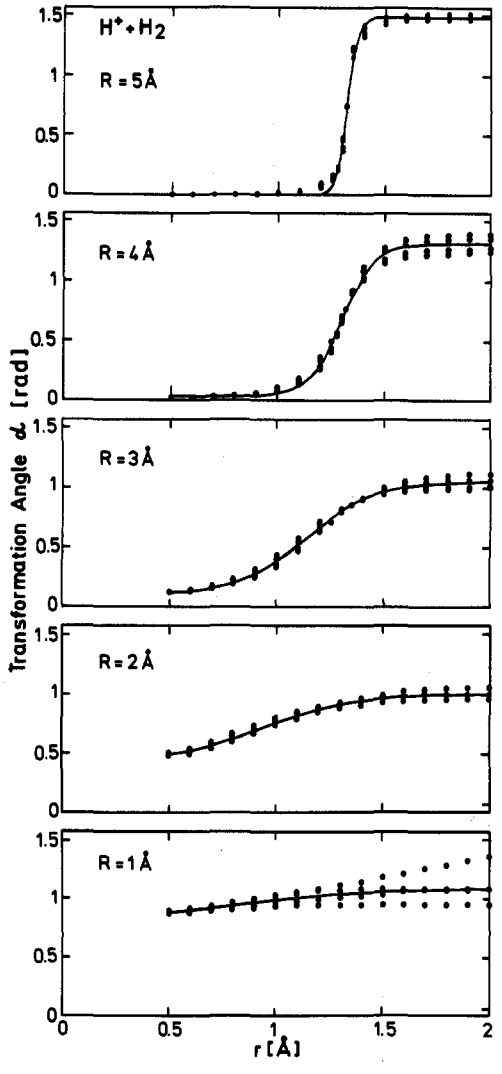

FIG. 2. The adiabatic diabatic transformation angle α as a function of the vibrational coordinate r for different values of the translational coordinate R. For each value of r α was calculated for $\gamma = 0°, 30°, 60°, 90°$. The full line is the analytic fit derived from Eq. (23).

B. The IOSA physical functions

The IOSA provides the following comparatively simple expressions for the observable differential and integral cross sections:

$$\frac{d\sigma^q}{d\Omega} = \frac{1}{8k_{v_i}^2}\sum_l\sum_{l'}(2l+1)(2l'+1)P_l(\cos\theta)P_{l'}(\cos\theta)$$
$$\times\int_{-1}^{+1} d(\cos\gamma)S^q(E,\gamma,l|v_i,v_f)S^{q^*}(E,\gamma,l'|v_i,v_f) \tag{25}$$

and

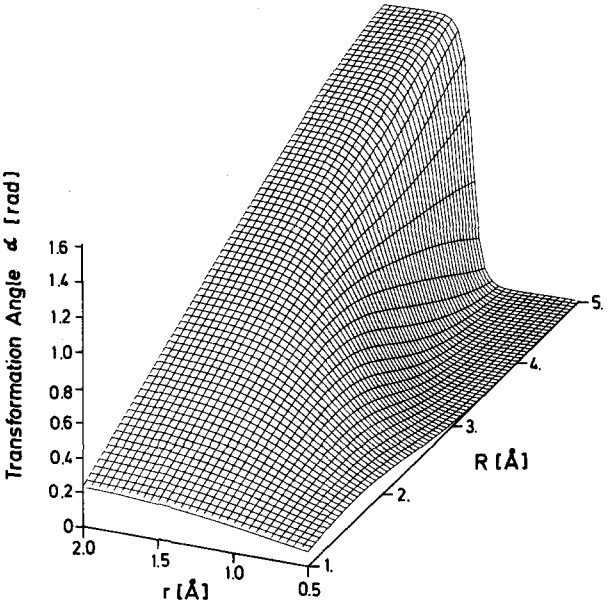

FIG. 3. A three-dimensional view of the analytical fit of the transformation angle α as a function of R and r. Note, that the fit is independent of the molecular orientation angle γ.

$$\sigma^q(E|v_i,v_f) = \frac{\pi}{2k_{v_i}^2}\sum_l (2l+1) \times \int_{-1}^{+1} d(\cos\gamma)|S^q(E,\gamma,l|v_i,v_f)|^2, \quad (26)$$

where E is the total energy, v_i and v_f are initial and final vibrational states, k_v is the initial wave vector, and S^q is the S matrix element obtained from the asymptotic wave function solution of Eqs. (18). The superscript q designates either the inelastic ($q = i$) or the charge transfer channel ($q = \mathrm{ct}$).

It is useful to calculate two additional quantities which although not experimentally accessible provide considerable insight into the kinematical details. One of these is the opacity function

$$P^q(E,l|v_i,v_f) = \frac{1}{2}\int_{-1}^{+1} d(\cos\gamma)|S^q(E,\gamma,l|v_i,v_f)|^2, \quad (27)$$

which is the probability that a given process, denoted by q, occurs as a function of the impact parameter related to the orbital angular momentum quantum number l, the initial vibrational state v_i and the final vibrational state v_f.

Secondly, the use of the IOSA makes it possible to define an orientation angle γ-dependent integral cross section which provides information on the steric effects:

$$\sigma^q(E,\gamma|v_i,v_f) = \frac{\pi}{k_{v_i}^2}\sum_l (2l+1)|S^q(E,\gamma,l|v_i,v_f)|^2. \quad (28)$$

IV. NUMERICAL DETAILS

All the calculations were carried out for an initial translational energy of $E_{\mathrm{cm}} = 20$ eV ($E_{\mathrm{lab}} = 30$ eV) and for $v_i = 0$ corresponding to the experimental conditions. For solving the coupled equations, Eqs. (18), the inclusion of altogether 25 vibrational states was found to be satisfactory. Of these 14 states were assigned to the lower surface and 11 states to the upper surface. The inclusion of additional vibrational states had no effect on the accuracy of the calculated cross sections. The coupled equations were solved for ten equally spaced values of γ (i.e., $\gamma = 0°$, 10°, 20°, ..., 90°) and altogether 251 l values where $l_{\max} = 250$ corresponds to $b \sim 3$ Å. The total computing time on a UNIVAC 1140 for a complete calculation was about 100 h.

Considerable effort was devoted to choosing the integration limits of r and R. Whereas the lower limit on $r_{\min} = 0.3$ Å is no problem because of the strong short range repulsion over the entire potential surface the choice of the upper limit has a significant effect on the results. The main requirement for $r_{\max}$ is, of course, that increasing its value will not change the final results. This is relatively easy to satisfy when a surface is not reactive but a reactive surface may cause difficulties in case a reactive channel has to be ignored. In fact, for the high energy of 20 eV considered here loss of flux into the reactive channel is not expected as was also verified in the recent TSH study.[13] Thus ignoring the flux into the reactive channel is not expected to affect the final cross sections if $r_{\max}$ is assumed to be large enough. Figures 4 and 5 show the

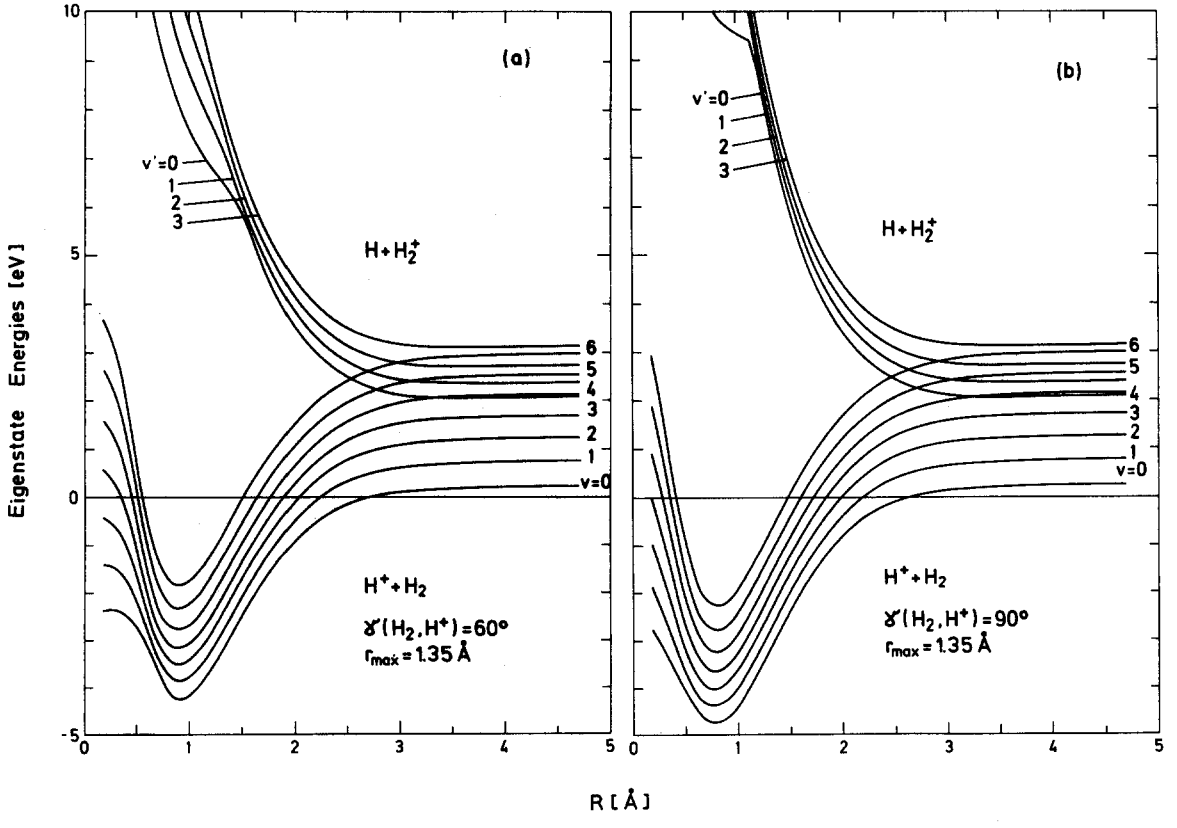

FIG. 4. Vibronic potential curves along the reaction coordinate for the two lowest quasiadiabatic surfaces. The calculations were carried out assuming $r_{\min} = 0.3$ Å and $r_{\max} = 1.35$ Å. (a) $\gamma = 60°$; (b) $\gamma = 90°$.

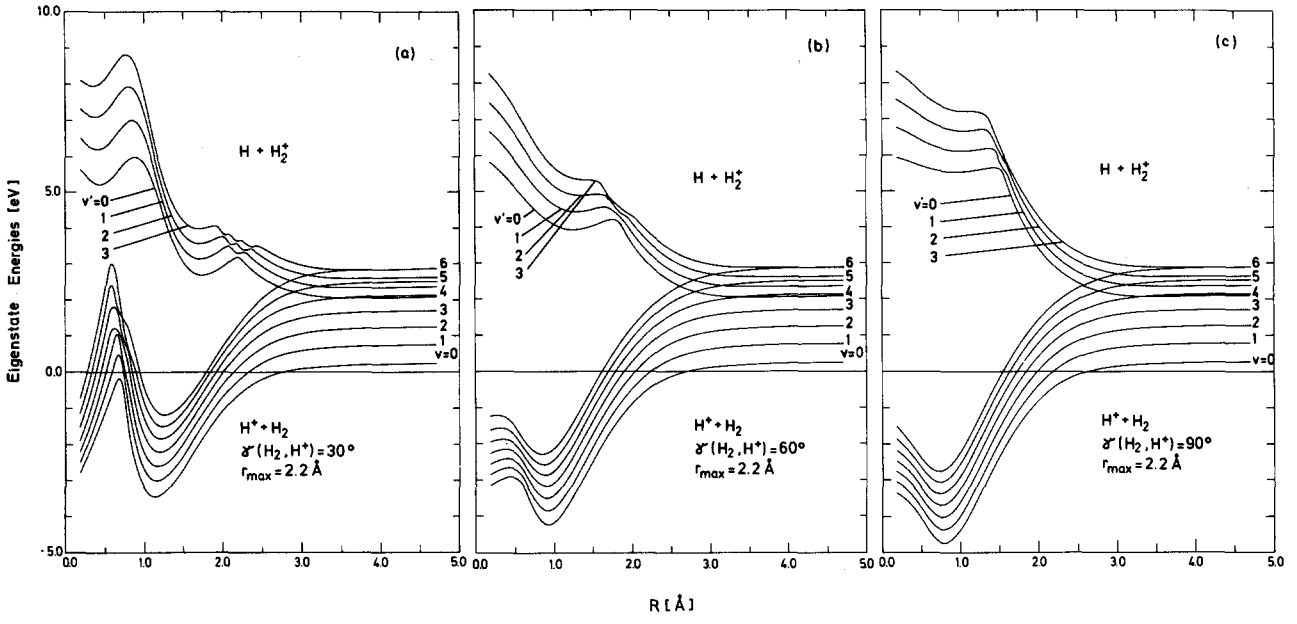

FIG. 5. The same as Fig. 4 but for $r_{max} = 2.2$ Å. (a) $\gamma = 30°$; (b) $\gamma = 60°$; (c) $\gamma = 90°$.

vibronic curves, of the two quasiadiabatic surfaces, along the translational coordinate R; the curves in Fig. 4 were obtained for $r_{max} = 1.35$ Å [the curves for $\gamma = 60$ are given in Fig. 4(a) and those for $\gamma = 90°$ in Fig. 4(b)] and the ones in Fig. 5 for $r_{max} = 2.2$ Å [the curves for $\gamma = 30°$, 60°, 90° are displayed in Figs. 5(a), 5(b), and 5(c) respectively]. Comparison of Figs. 4 and 5 illustrates the effect of the two choices of r_{max} on the structure of the vibronic curves of the lower surface. These differences are in fact large enough to significantly affect the final calculated S-matrix elements. The close coupling calculations were carried out for different values of r_{max} and the results were found not to vary for $r_{max} \geqslant 2.2$ Å.

Another difficulty associated with the reactive nature of the surface is the fact that vibronic curves of the lower surface do not increase as R decreases. As a result the initial value of R, R_{min}, has to be chosen very close to zero, i.e., $R_{min} < 0.1$ Å. Unfortunately such small values of R cause numerical instabilities and consequently R_{min} could not be chosen smaller than 0.4 Å. As a consequence our calculations cannot be entirely trusted for l values in the range $0 \leqslant l \leqslant 20$. When l becomes larger, the inner portion of the potential is entirely screened by the centrifugal potential, and thereby this difficulty disappears. As our main interest is in the forward direction, i.e., $0° \leqslant \theta \leqslant 20°$ this does not affect any of the differential cross sections and conclusions presented here. For the integral cross sections the resulting relative error is not expected to be larger than 5%. As for the upper value of R, R_{max}, no difficulties were encountered and it was assumed to be 4.7 Å.

The differential cross sections showed considerable undulatory structure as a function of scattering angle which can be explained by various quantum interference effects including fast oscillations. Since the present experiment is not able to resolve these effects the calculated angular distributions were smoothed for reasons of clarity by folding them with a Gaussian distribution:

$$\frac{d\bar{\sigma}}{d\Omega}(\theta) = A \int_{\bar{\theta}-\Delta\theta}^{\bar{\theta}+\Delta\theta} \exp\left[-\frac{(\theta-\bar{\theta})^2}{2\sigma_\theta^2}\right] \frac{d\sigma}{d\Omega}(\theta) d\theta, \quad (29)$$

where $\Delta\theta = 1°$, $\sigma_\theta = 0.33°$, and A is a normalization factor.

V. RESULTS

A. Inelastic differential cross sections

To assess the overall accuracy of the IOSA, differential cross sections for the vibrationally inelastic channel were calculated for the ground potential surface and compared with the experiment. The results are shown in Fig. 6(a) for $v_f = 0$, 2, 4, and 6 and in Fig. 6(b) for $v_f = 1$, 3, and 5. An earlier comparison of the same experimental results with TSH calculations,[13] for some representative v_f states, is shown in Fig. 6(c) and (d). These latter calculations were also based on the same DIM potential surface. Since the experiment only provides relative cross sections they were arbitrarily matched to the theoretical cross section as in the previous paper[13] by setting the experimental $v_f = 0$ cross section equal to the theoretical cross section at a scattering angle of $\theta = 7°$.

The main observed discrepancy between theory and experiment is with respect to the position of the rainbow angle. It is noticed that the rainbow scattering angles calculated with IOSA are all shifted by about 2.5° towards larger angles. This discrepancy is somewhat of a surprise because in previous approximate quantum mechanical calculations of vibrationally inelastic cross sections in which both the reactive and the charge transfer channels were left out, the theoretical positions of the rainbow fit always the experimental value.[28–31] It should be mentioned that most of these were based

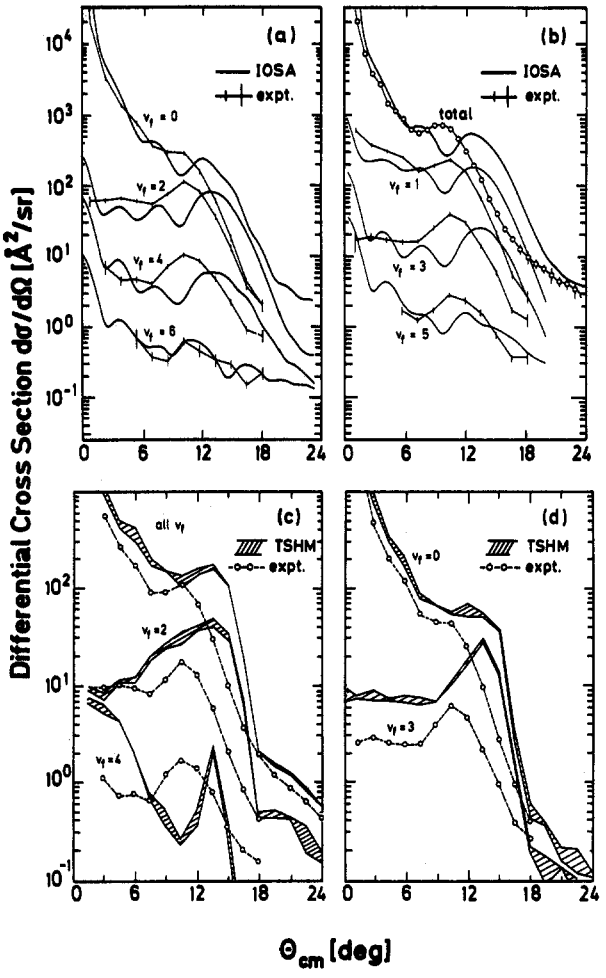

FIG. 6. Vibrational state-to-state elastic and inelastic differential cross sections. (a) and (b) give a comparison of the IOSA calculations with the experiments, whereas (c) and (d) present TSHM calculations (Ref. 13). The experimental curves are shown as straight line segments connecting the individual points with the error bars. The IOSA calculations are shown as smooth lines, the TSHM calculations as hatched areas, respectively. Since absolute cross sections could not be measured the experimental data were arbitrarily normalized to fit the theoretical data. This has been done by multiplying all experimental curves with one parameter to fit the IOSA data and by one parameter to fit the TSHM data. Both parameters differ by a factor of 5 because the IOSA results and the TSHM results predict different sizes for the cross sections. Nevertheless, the behavior of all the cross sections around the rainbow is unambiguous: All theoretical curves show a shift of the rainbow by 1.5 to 2 deg towards larger angles with respect to the experimentally observed rainbow.

on either IOSA or simpler approximations so that the reason of the present discrepancy is probably not associated with the dynamic approximation. Confirmation of the present result is found in the recent TSH studies[13] (see also Ref. 32) where, essentially, the same shift was observed.

A possible explanation for the differences in the two quantum calculations is as follows: in all previous quantum calculations[28–31] the range of the vibrational coordinate r was limited to $r_{max} = 1.35$ Å. In this way not only was the reactive channel eliminated but also the necessity to deal with the adiabatic–diabatic character of the surface was avoided since the position of the seam is at $r = 1.32$ Å. We showed above that the choice of r_{max} has a significant effect on the electrovibronic curves (see Figs. 4 and 5). Therefore r_{max} has to be chosen large enough so that any further increase will not affect the main diabatic potential curves and the final results will remain unchanged. In the present study it was found that the value of $r_{max} = 2.2$ Å is satisfactory. Thus the previous fit of the position of the rainbow angle between theory and experiment could very well be fortuitous. In the TSH studies the adiabatic potential energy surface is used directly without any restrictions on the range in r and consequently the reactive character of the surface, as in our quantum mechanical study, is fully accounted for.

In other respects the agreement between the IOSA calculation and the experiments is quite good. The IOSA calculation predicts the correct relative magnitude of the inelastic cross section all the way up to $v_f = 6$. If shifted by 2.5° to smaller angles, the IOSA also nicely reproduces the overall shape of the cross section at angles smaller than the rainbow and even suggests that some of the predicted oscillations may also be present in the experimental distributions. At small angles the agreement of the IOSA calculation with experiment is also better than for the semiclassical calculations of Krüger and Schinke[29] which show a steep decrease at $\theta < 2°$. Nevertheless, the strong peak of the IOSA calculations at $\theta = 0°$ remains unexplained. It may be due to the incorrect long range shape of the DIM potential matrices.

B. Charge transfer differential cross section

Figure 7(a) shows a comparison of the calculated charge transfer cross sections with the experiments. Figure 7(b) compares the same experimental results with the TSH calculation. As in the inelastic case the IOSA rainbow is shifted by about 2.5° to larger angles. The same shift is expected but not apparent in the TSH calculations. The relative cross sections for the final vibrational states are once more nicely reproduced by the IOSA calculations and are also in better agreement with experiment than the TSH predictions. At small angles $\theta \lesssim 3°$ there is a serious disagreement between theory and experiment where the present IOSA and the TSH theories both predict an increase in cross sections, whereas the experiment shows a falloff. In evaluating the experiments the overall shape of the differential cross section had to be corrected for a spurious signal resulting from charge transfer collisions with the residual gas background. Since this background signal can be clearly resolved in the TOF distribution this correction should be quite accurate and therefore the small angle discrepancy seems to be real. We will discuss possible explanations in the final section.

Figure 7 clearly shows that the IOSA provides a better description of the experimental results than the TSH theory. This becomes even more apparent when the total differential cross sections are compared as shown in Fig. 8. Since both theories provide absolute cross sections the magnitudes can be compared directly, revealing that the TSH cross sections are too small by nearly an order of magnitude. For comparison with the experimental cross sections, which are only relative, an arbitrary normalization had to be introduced. In this case the magnitude of the experimental cross section was matched to the IOSA cross section at the rainbow angle. The reason for the differences between IOS and TSH absolute

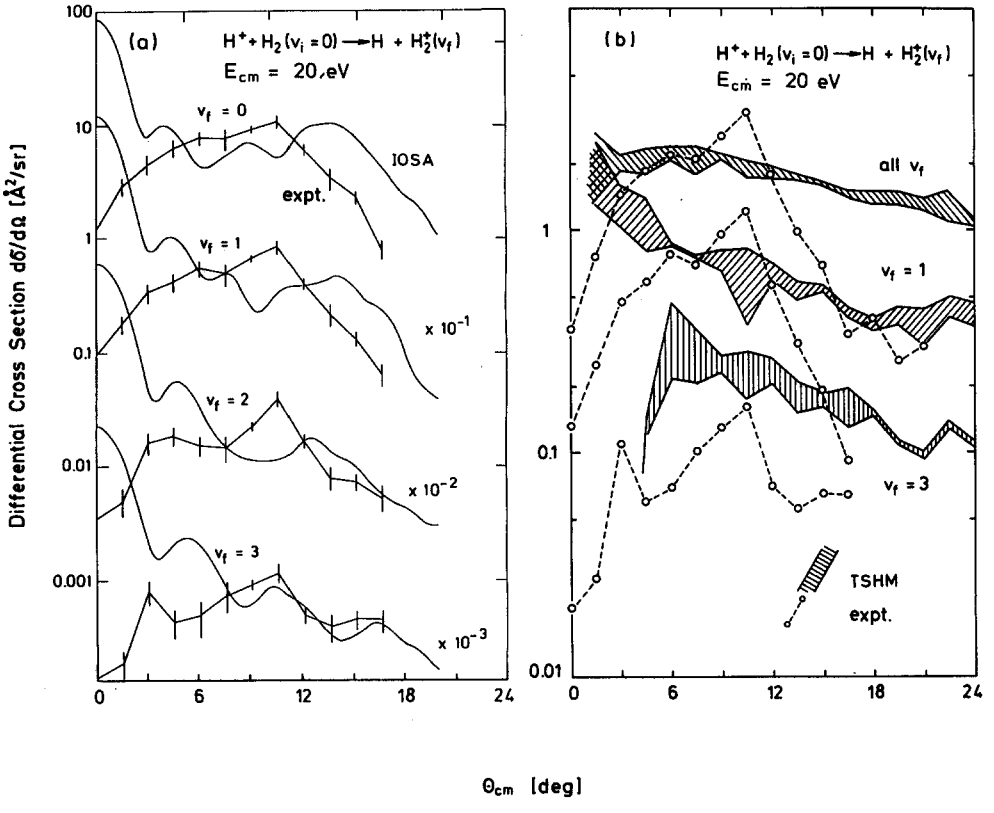

FIG. 7. Vibrational state-to-state charge transfer differential cross sections. (a) gives a comparison of the IOSA calculations (smooth lines) with the experiments (straight line segments with error bars), whereas (b) gives the same experimental data again (open circles, connected with dashed lines) together with the TSHM data (hatched areas). Normalization of the experimental curves is done as described in Fig. 6. For reasons of clarity the data in (a) have been shifted by various factors as indicated on the right side of the figure. Although the same angular shift as in Fig. 6 is observed with respect to the position of the rainbow the IOSA calculations reproduce the experimental rainbow in general, whereas all the TSHM curves are unstructured and flat.

cross sections will become more apparent from the discussion of the opacity functions.

C. Average energy transfers and integral cross sections

The experimental time of flight spectra when converted to an energy loss abscissa provide a direct measure of the energy loss distributions. This distribution can be characterized by its moments, where the first moment will be referred to as the average energy transfer $\Delta E^{(1)}$. For $H^+ + H_2$ it is found that $\Delta E^{(1)}$ agrees within a few percent with the value calculated from the relative vibrational transition probabilities:

$$\Delta E_{\text{vib}}^{\text{inel.}} = \sum_f P(i \rightarrow f) \Delta E(i \rightarrow f), \tag{30}$$

where $P(i \rightarrow f)$ are the relative vibrational inelastic probabilities normalized to one and $\Delta E(i \rightarrow f)$ are the vibrational energy level differences. Equation (30) can be applied equally to the inelastic and the charge transfer channels. In both cases the values of $\Delta E^{(1)}$ and $\Delta E_{\text{vib}}^{\text{inel.}}$ agreed to within few percent indicating that the contribution from unresolved vibrational energy transfer and rotational excitation amounts to only a few percent of $\Delta E^{(1)}$. The observed small amount of rotational excitation provides an additional justification for the use of the IOSA.

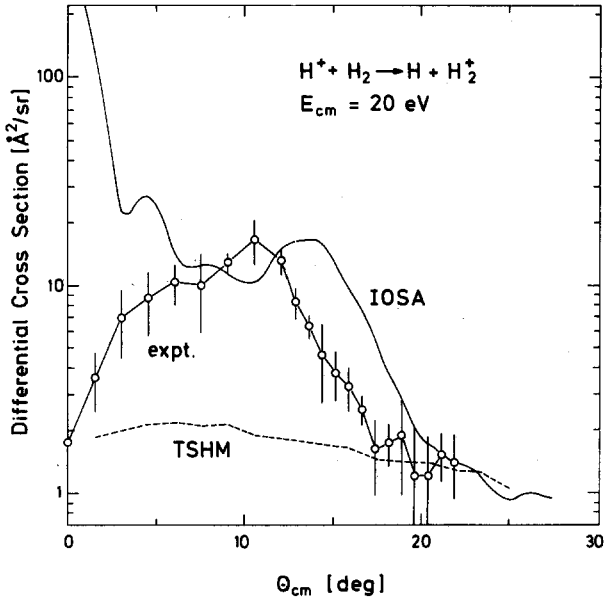

FIG. 8. Total charge transfer differential cross sections. A comparison between theoretical (IOSA and TSHM) and experimental results. The experimental curve is shifted in such a way that its maximum coincides with the IOSA maximum at their corresponding rainbow angles.

Figure 9(a) presents a comparison of the experimental $\Delta E^{(1)}$ values as a function of laboratory scattering angle with both the TSH and IOSA calculations. In this case the agreement of the experiment with both theories is quite good, with the experimental results lying nearly halfway between the two theoretical curves. Figure 9(b) shows the analogous comparison for the charge transfer channel and again the agreement with both theories is quite satisfactory. At $\theta_{\text{lab}} \geqslant 5°$ it even appears as if the IOSA provides a somewhat better fit of the experiment than the TSH theory, whereas at smaller angles, neglecting the angular region $\theta < 2°$, a clear preference for one of the two theories is not so clear.

State-to-state integral cross sections although not di-

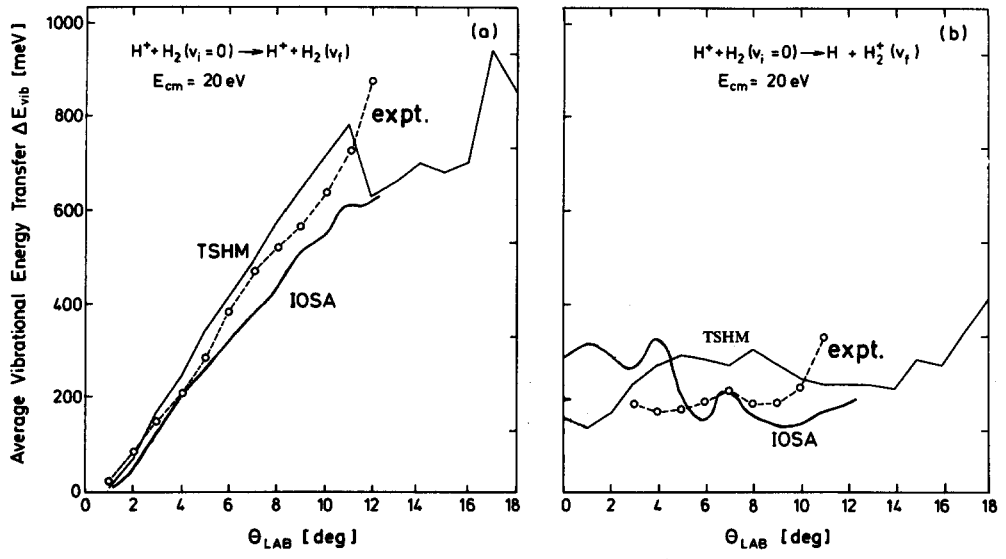

FIG. 9. Comparison of average vibrational energy transfer as a function of the scattering angle calculated from the TSHM and IOSA approximation with the experimental results. (a) For inelastic processes; (b) for charge transfer processes. In case of (b) the value of 1.83 eV has been subtracted off to account for the endothermicity.

rectly measured in the apparatus can be derived from the differential cross sections. The procedure requires an integration of the angular distributions out to the largest angle. In the present study the detector probed only a limited angular range, i.e., $0° \leqslant \theta \leqslant 18°$, and consequently only incomplete integral cross sections could be obtained. However, since this range includes the rainbow, most of the contributions to the inelastic and charge transfer processes are expected to come from this region. This assumption was checked by integrating the IOSA differential cross sections over the entire angular range and comparing with the cross sections obtained by integrating just beyond the rainbow region. The results are compared in Table I and it is seen that, whereas most processes indeed take place inside the rainbow region, contributions from the larger angular region cannot be ignored. In particular, it is noticed that 40% of the charge transfer processes occur in the angular region beyond the rainbow.

The experimental incomplete integral cross sections as a function of v_f are shown in Figs. 10(a) and 10(b) where they are compared with the two theories. For the inelastic case the experiments were adjusted to match the theoretical absolute values for $v_f = 0$ where both theories predict very similar values. It is seen that the IOS calculation agree almost perfectly with the observed rapid decrease in cross section with v_f, whereas the TSH calculations are not nearly as good. For the charge transfer case the experiments were adjusted to match the IOSA $v_f = 0$ result and an excellent agreement in the dependence of v_f is found. As discussed previously neither of the two theories nor the experiment come close to the distributions expected from the commonly used Franck–Condon factors.

Finally in Table I the absolute cross section calculated with the IOSA are listed. The total integral cross section for charge transfer is found to be 1.1 Å^2. The closest available experimental result is $\sigma = 0.226$ Å^2 at $E_{cm} = 50$ eV.[33] Assuming that the charge transfer cross section decreases as E_{cm}^{-1} it is estimated to be 0.57 Å^2 at $E_{cm} = 20$ eV which is about one half of the IOSA value. The agreement is considered satisfactory in view of the approximation nature of the potential surface. At the same energy (i.e., $E_{cm} = 20$ eV) the TSH theory predicts a value of 0.3 Å^2.

TABLE I. IOSA $v_i = 0$ to v_f state-to-state and total integral cross sections for inelastic (elastic) and charge transfer processes at $E_{cm} = 20$ eV as a function of v_f. The numbers in parentheses are the corresponding incomplete integral cross sections calculated for the angular range $0 < \theta_{cm} \leqslant 18°$.

Final vibrational state v_f	Cross sections (Å^2)	
	Inelastic	Charge transfer
0	52.4 (52.4)	0.53 (0.36)
1	5.3 (5.3)	0.33 (0.23)
2	2.2 (2.06)	0.16 (0.10)
3	0.77 (0.68)	0.088 (0.044)
4	0.27 (0.209)	···
5	0.13 (0.076)	···
6	0.065 (0.026)	···
Total	61.1 (60.75)	1.10 (0.73)

VI. DISCUSSION

One attractive feature of the IOSA is that it provides considerably more insight into the details of the microscopic dynamics than is readily available with a full close coupling calculation. The decoupling of the angular momenta means that the IOSA opacity function can be compared directly with TSH probability distributions calculated as a function of b.

In Fig. 11 we first present the IOSA opacity function for the total charge transfer process and for most of the values of v_f accessed in inelastic collisions. As it is well known that opacity functions are very oscillatory, for reasons of clarity, all the distributions were smoothed by a five point sliding average over l. The cross section for $v_i = 0 \rightarrow v_f = 0$ and the total cross section both show the typical semiclassical undulation which at $l \simeq 190$ corresponds to the rainbow and supernumerary rainbows. These supernumerary rainbows, al-

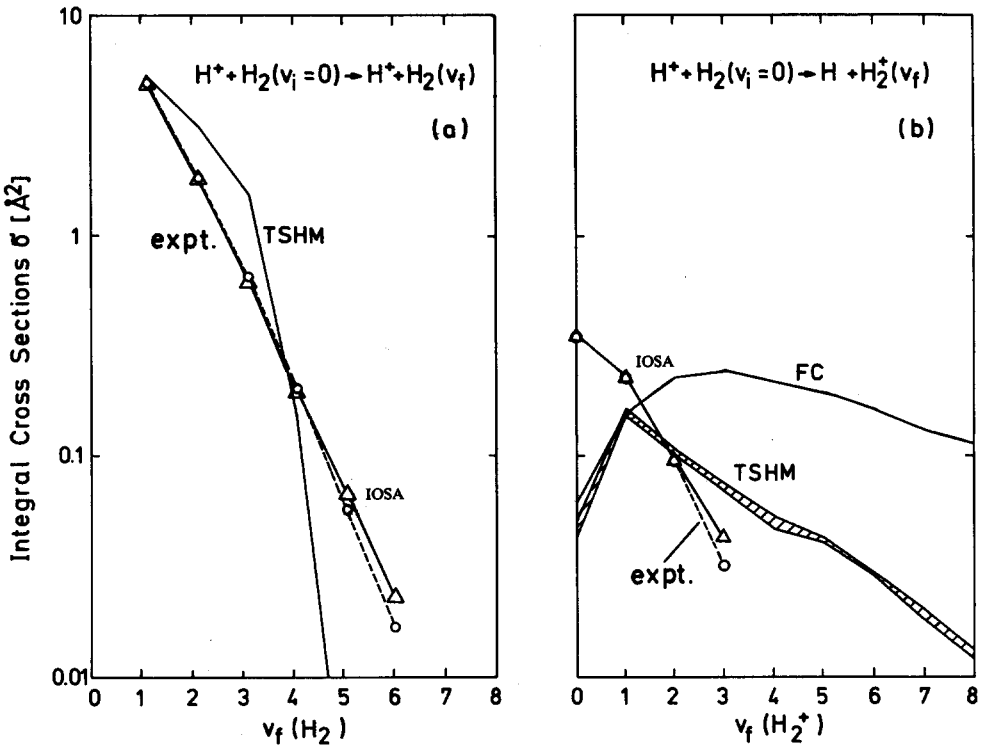

FIG. 10. A comparison between experimental and theoretical incomplete integral vibrational distribution (see Table I). (a) Inelastic process. (b) Charge transfer process.

though not clearly resolved in the present experiments have been, however, nicely resolved at lower collision energies. It comes somewhat as a surprise that the $v_f = 1$ and $v_f = 2$ channels do not show similar undulations. At $v_f = 3$ and especially at $v_f = 4$ and 5 the inelastic state to state cross sections show a new sequence of oscillations of higher frequency than seen in the total cross section. These oscillations are probably due to Stueckelberg oscillations[27] since charge transfer is expected for $v_f \geqslant 4$. It is interesting to see that although the $v_f = 3$ state lies below the threshold for charge transfer it also exhibits the same type of oscillatory behavior. This is not unexpected in view of the close proximity of the $v_f = 3$ energy level to that of the charge transfer channel and the energetic smearing allowed by quantum mechanics. From Fig. 11 it can also be seen that the charge transfer cross sections and the inelastic cross sections are out-of-phase. This is attributed to the very strong coupling between the $v_f \geqslant 4$ inelastic channels and the charge transfer channel.

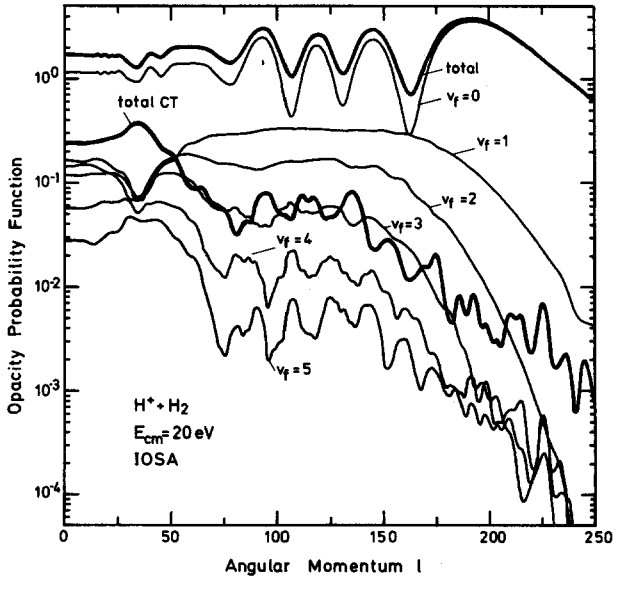

FIG. 11. Smoothed IOSA calculated opacity probabilities as a function of the orbital angular momentum quantum number l. The inelastic and the *total* charge transfer opacity functions are shown.

The opposing phases seen in the opacity functions for the two processes disappear in a comparison of differential cross sections, shown in Fig. 12. The angular distributions for the inelastic $v_f = 4$ cross section and the dominant $v_f = 0$ charge transfer cross section are now found to be in phase. This result is also consistent with the strong coupling between the two channels. According to the interpretation in our earlier paper on $H^+ + Xe$[34] the outgoing wave packet of inelastically scattered systems when passing through an avoided crossing will divide into two components moving on both surfaces with equal probability. Thus both channels are expected to show very similar angular distributions. The bottom two experimental curves in Fig. 12 show that this is indeed seen in the experiments. The difference in shape between experiment and theory has already been discussed in the previous section.

The opacity function can also be compared directly with the probability functions calculated with the TSH method. This is shown in Figs. 13 and 14, and it points out some important differences between the two approximations. The IOSA, unlike the TSH calculation, predicts that charge transfer, which is indicated by the dark areas in Fig. 13, occurs over a wide range of impact parameters namely for $0.0 \leqslant b \leqslant 2.5$ Å [the relation between b and l, at this energy, is $b = 0.0125\, l$ (Å)]. In the TSH model charge transfer occurs

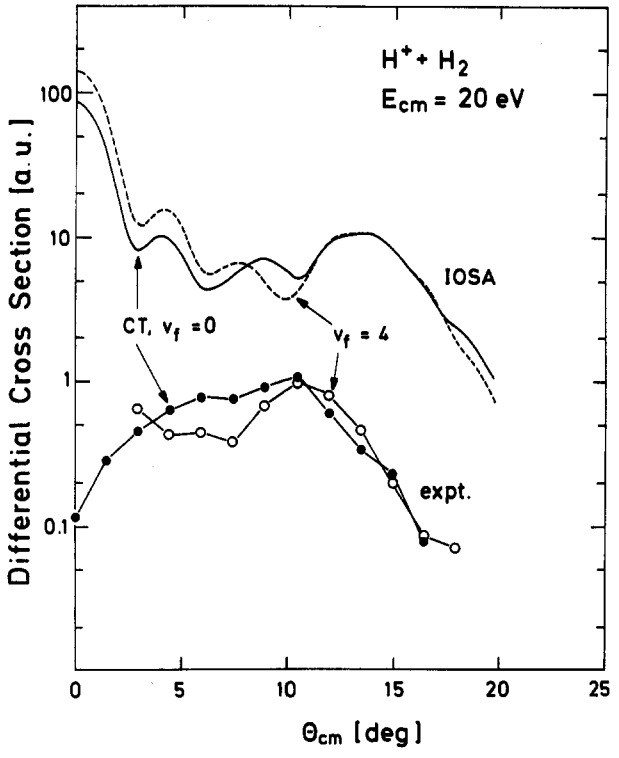

FIG. 12. Comparison of the differential cross sections for the inelastic vibrational transition $v_i = 0 \rightarrow v_f = 4$ with the differential cross section of the charge transfer process $v_i = 0 \rightarrow v_f = 0$. Although the IOSA results and the experimental data show some differences, both the experimental and the IOSA curves are that similar with respect to themselves, that a strong coupling between the inelastic scattering into $H_2(v_f = 4)$ and the charge transfer can be claimed to be proofed thereby.

almost entirely in the small impact region (see Fig. 14). The failure of the TSH theory in reproducing the experimental charge transfer rainbow was already discussed in connection with Figs. 7(b) and 8 and was also noted in an earlier publication.[13] There it was attributed to uncertainties in the DIM potential. The present comparison with the IOSA calculations for the same surface indicates that this explanation has to be dropped. Further, it suggests that the surface hopping method for treating transitions between surfaces leads to serious errors. We will return to this issue in the final section. The fact that the TSH calculations do not duplicate the interference undulations seen in the same impact region in the IOSA calculation is, of course, expected.

According to the TSH model charge transfer takes place mainly along the short impact range where direct, almost head-on, collisions take place. According to the IOSA charge transfer happens along the whole relevant impact parameter range but with varying probability. In Fig. 15 the various opacity functions are presented on a linear scale to emphasize the relative probabilities along b. Although by far the largest charge transfer probabilities are obtained for short range impact parameters, the weighting of the probabilities by the impact parameter to form cross sections evens out the contributions from all regions.

Steric effects can also be obtained from the present IOSA study by examining the γ dependent cross sections [see Eq. (28)]. Figure 16(a) shows the vibrational state-to-state inelastic cross sections and Fig. 16(b) those accompanied with charge transfer. The two kinds of results exhibit a moderate dependence on γ with variations of 20%–50%. The dependence on γ for inelastic processes is anticipated because the position of the classical turning point, even for relatively large values of l, is expected to depend on γ [see Figs. 1(d) and 1(e)]. As for charge transfer, although it takes place far away from the classical turning point and

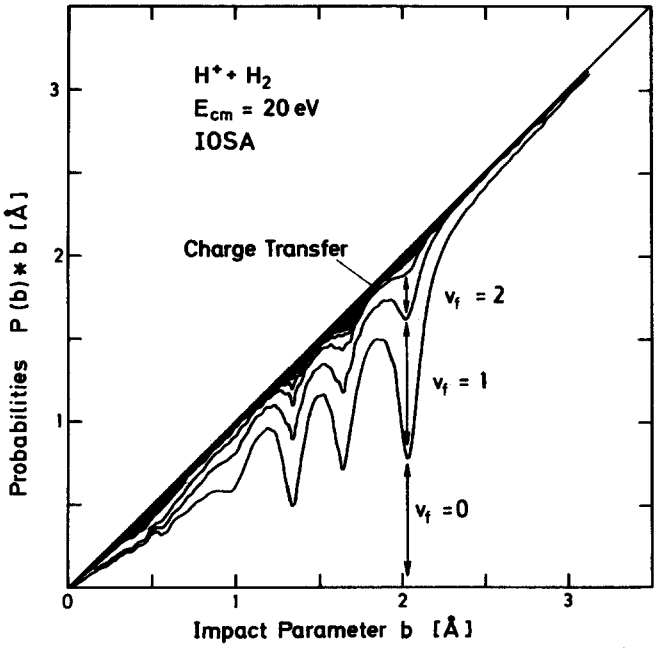

FIG. 13. IOSA weighted opacity functions $b \cdot P_i(b)$ as a function of impact parameter b. The area between each two adjacent curves represents the relative contribution of the ith process to the total cross section. Thus the area under the lowest curve represents the contribution of the elastic process, the area between the first two curves represents the contribution of the inelastic $v_i = 0 \rightarrow v_f = 1$ process, etc. The darkened area represents the contribution of the charge transfer process. Note that the straight line represents $F(b) = b \sum P_i(b) = b$ [because $\sum P_i(b) = 1$].

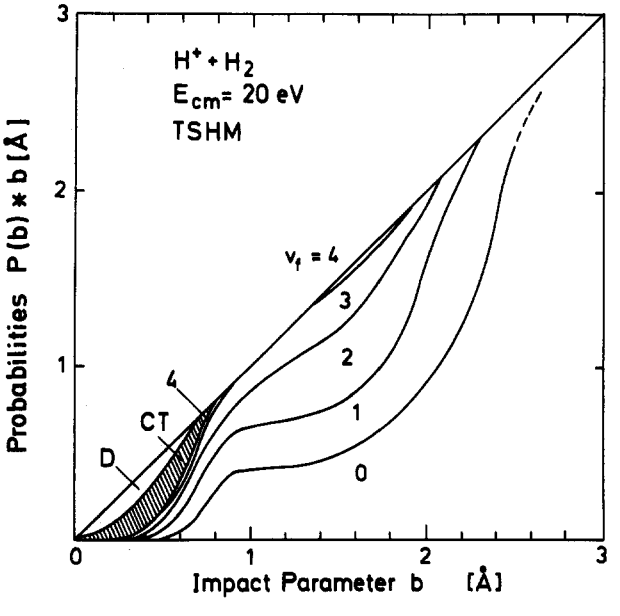

FIG. 14. TSHM calculated probability functions $b \cdot P_i(b)$ as a function of the impact parameter b. For general explanation see Fig. 13. Charge transfer takes places only for impact parameters up to $b_{max} = 0.8$ Å.

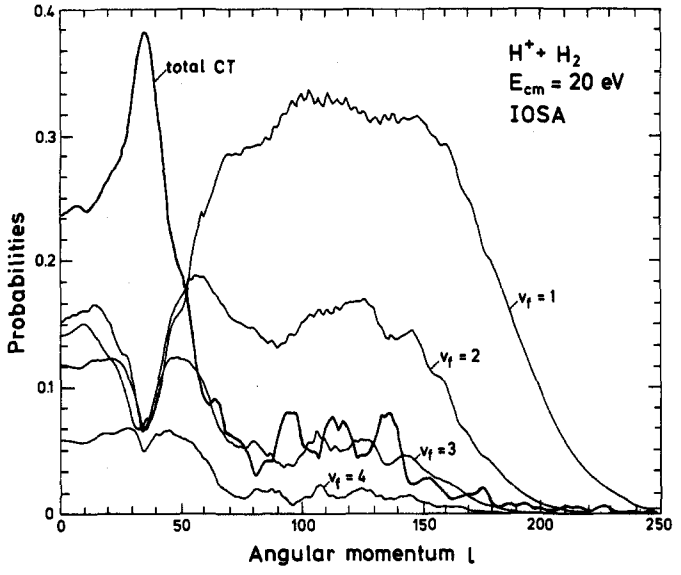

FIG. 15. IOSA-opacity functions on a linear scale. The data of Fig. 14 (log scale) are presented on a linear scale to emphasize the strong occurrence of charge transfer around $l = 35$.

although the nonadiabatic coupling terms are found not to depend on γ, still variations of 20%–30% in the cross sections were observed. This can be explained by the strong coupling between the vibrational inelastic excitations, which are γ dependent, and the charge transfer process.

Moreover, it is noticed that $\sigma^{ie}(\gamma|v_f = 2)$ as well as $\sigma^{ie}(\gamma|v_f = 1)$, which is not shown, both depend on γ differently than $\sigma^{ie}(\gamma|v_f \geqslant 3)$. Whereas the latter decrease earlier with increase of γ—the decrease starts at $\gamma = 20°$—the former starts to decrease later, i.e., at $\gamma \geqslant 60°$. The $\sigma^{ct}(\gamma|v_f)$ curves in Fig. 16(b) exhibit an oscillatory behavior such that their maximum appears around $\gamma \sim 50°$. Thus, it seems that the missing portion of the $\sigma^{ie}(\gamma|v_f \geqslant 3)$ curves is recovered in the $\sigma^{ct}(\gamma|v_f)$ curves. The fact that the charge transfer process affects the excitation of $v_f \geqslant 4$ is expected due to the Fermi type resonances between the vibronic states of the lower and the upper surfaces [see Ref. 11(b) and Fig. 4] but here we have an indication that also the excitation to $v_f = 3$, which is much lower than the ground state of the upper surface ($\Delta E \sim 0.35$ eV), is also significantly affected.

As a final result we refer to the γ dependence of the average energy transfer (Fig. 17) for inelastic scattering as well as for charge transfer. Whereas only a weak dependence on γ is observed for the inelastic process a strong dependence is observed for the charge transfer. The reason for this different behavior is not understood.

VII. SUMMARY

The IOSA calculations have been found to be in agreement with the following: (a) The angular distribution of each final vibrational state of product molecules $H_2(v_f)$, resulting from an inelastic collision and $H_2^+(v_f)$, resulting from charge transfer. (b) The relative yield for both processes. (c) The location of the rainbow angles for both the inelastic and the charge transfer processes.

Two disturbing discrepancies still remain between theory and experiment: (a) The first relates to the position of the rainbow angle. The theoretical position, like the positions obtained previously in classical and semiclassical studies, is

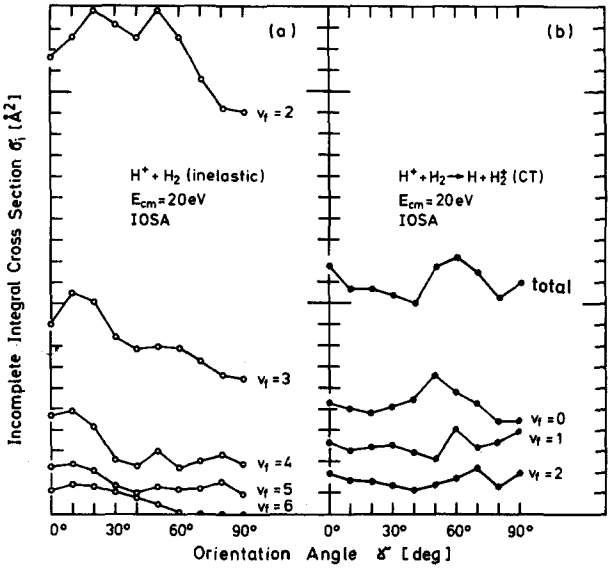

FIG. 16. γ-dependent state-to-state integral cross sections. (a) Inelastic transitions. (b) Charge transfer transitions.

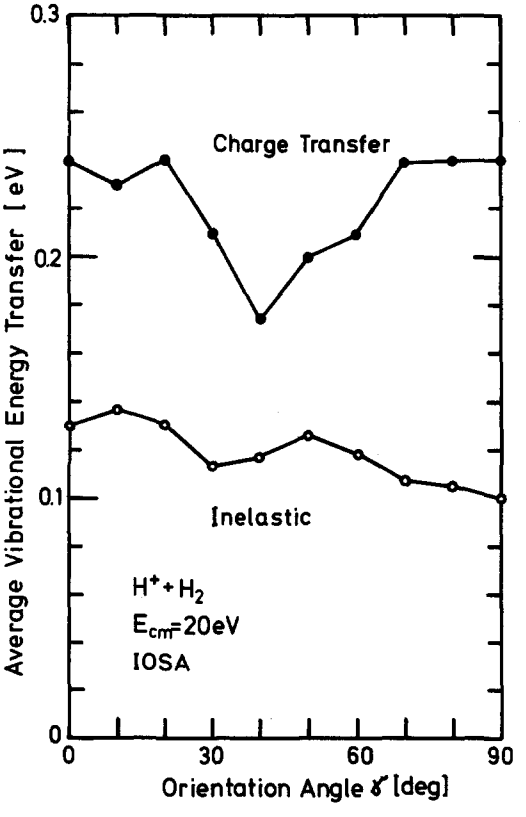

FIG. 17. IOSA calculated average vibrational energy transfer as a function of the orientation angle γ.

found to be shifted by 2.5° towards the larger angles. It is difficult to attribute this discrepancy to uncertainties concerning the potential well, because the potential well is believed to be known rather accurately. Hence, this difference remains an unresolved problem. (b) The theoretical charge transfer differential cross sections differ significantly from the experimental cross sections for $\theta < 2°$. Whereas the latter decrease as θ approaches zero the former increase. This discrepancy might be due to errors in the long range potential employed in our study, since the long range induced dipole term was not included.

An interesting outcome of this study concerns the details of charge transfer in this system. Considering the opacity probability functions, we found that charge transfer takes place over most of the entire impact parameter range, but with varying probabilities. For small impact parameters unusually high charge transfer probabilities (sometimes as high as 40%) are encountered similar to those in the TSHM study.[13] However, they occur only for a short range, i.e., $b \ll 1$ Å. In the rainbow region, the probabilities are much smaller ($< 10\%$) but apply for a wide range of impact parameters. The charge transfer process is expected to occur following strong inelastic excitations on the lower surface[11(b),13] as illustrated by the close correlation of the behavior of the two resonant inelastically scattered excited $H_2(v = 4)$ molecule and the charge transferred H_2^+ ($v = 0$) molecule.

The present study revealed some shortcomings of the TSHM. Not only does TSHM incorrectly predict the angular distribution for the products (no rainbow structure and the wrong vibrational distribution), but it also yielded an incorrect vibrational distribution for the inelastic collisions. Thus for instance the relative population of $v_f = 2$ was more than 50% off and that of $v_f = 3$ more than 100% off. We also found that the integral total TSHM charge transfer cross section was about 50% smaller than the IOSA cross section, mainly because contributions from the rainbow region were lacking.

ACKNOWLEDGMENT

We thank Ch. Schlier for providing us with the DIM potential matrix.

[1] M. Baer, in *The Theory of Chemical Reaction Dynamics*, edited by M. Baer (Chemical Rubber, Boca-Raton, FL, 1985), Vol. II, Chap. IV.
[2] M. S. Child, in *Atom–Molecule Collision Theory*, edited by R. B. Bernstein (Plenum, New York, 1979), p. 427.
[3] J. C. Tully, in *Dynamics of Molecule Collisions*, Part B, edited by W. H. Miller (Plenum, New York, 1976), p. 217.
[4] E. Bauer, E. R. Fisher, and F. R. Gilmore, J. Chem. Phys. **51**, 4173 (1969).
[5] A. Bjerre and E. E. Nikitin, Chem. Phys. Lett. **1**, 179 (1967).
[6] S. Chapmann, J. Chem. Phys. **82**, 4033 (1985).
[7] Ch. Schlier, V. Nowotny, and E. Teloy, Chem. Phys. **111**, 401 (1987).
[8] L. D. Landau, Phys. Z. Sowjetunion **1**, 88 (1932); ibid. **2**, 46 (1932).
[9] C. Zener, Proc. R. Soc. London Ser. A **137**, 696 (1932).
[10] M. Baer, Chem. Phys. Lett. **35**, 112 (1975); Chem. Phys. **15**, 49 (1976).
[11] (a) Z. H. Top and M. Baer, J. Chem. Phys. **66**, 1363 (1977); (b) Chem. Phys. **25**, 1 (1977).
[12] M. Baer and H. Nakamura, J. Chem. Phys. **87**, 4651 (1987).
[13] G. Niedner, M. Noll, J. P. Toennies, and Ch. Schlier, J. Chem. Phys. **87**, 2685 (1987).
[14] (a) R. K. Preston and J. C. Tully, J. Chem. Phys. **54**, 4297 (1971); (b) J. C. Tully and R. K. Preston, *ibid.* **55**, 562 (1971).
[15] F. O. Ellison, J. Am. Chem. Soc. **85**, 3540, 3544 (1963).
[16] R. Schinke, M. Dupuis, and W. A. Lester, J. Chem. Phys. **72**, 3909 (1980).
[17] J. Tennyson and B. Sutcliffe, Mol. Phys. **51**, 887 (1984).
[18] W. Meyer, P. Botschwina, and P. Burton, J. Chem. Phys. **84**, 891 (1986).
[19] F. T. Smith, Phys. Rev. **179**, 111 (1969).
[20] M. Born and J. R. Oppenheimer, Ann. Phys. (Leipzig) **84**, 457 (1927).
[21] L. Monchick and E. A. Mason, J. Chem. Phys. **35**, 1676 (1961).
[22] K. H. Kramer and R. B. Bernstein, J. Chem. Phys. **40**, 200 (1964).
[23] D. Secrest, J. Chem. Phys. **62**, 710 (1975).
[24] T. P. Tsien, G. A. Parker, and R. T. Pack, J. Chem. Phys. **59**, 5373 (1973).
[25] D. J. Kouri, in Ref. 2.
[26] M. Baer and H. Nakamura, J. Phys. Chem. **91**, 5503 (1988).
[27] E. C. G. Stückelberg, Helv. Phys. Acta **5**, 369 (1932).
[28] P. McGuire, J. Chem. Phys. **65**, 3275 (1976).
[29] H. Krüger and R. Schinke, J. Chem. Phys. **66**, 5087 (1977).
[30] R. Schinke, Chem. Phys. **24**, 379 (1977).
[31] R. Schinke and P. McGuire, Chem. Phys. **28**, 129 (1978); **31**, 391 (1978).
[32] C. F. Giese and W. R. Gentry, Phys. Rev. A **10**, 2156 (1974).
[33] W. H. Cramer, J. Chem. Phys. **35**, 836 (1961).
[34] M. Baer, R. Düren, B. Friedrich, G. Niedner, M. Noll, and J. P. Toennies, Phys. Rev. A **36**, 1063 (1987).